

Power generation from ambient humidity using protein nanowires

<https://doi.org/10.1038/s41586-020-2010-9>

Received: 19 November 2018

Accepted: 14 November 2019

Published online: 17 February 2020

 Check for updates

Xiaomeng Liu¹, Hongyan Gao¹, Joy E. Ward², Xiaorong Liu³, Bing Yin¹, Tianda Fu¹, Jianhan Chen^{3,4,5}, Derek R. Lovley^{2,4} & Jun Yao^{1,4}✉

Harvesting energy from the environment offers the promise of clean power for self-sustained systems^{1,2}. Known technologies—such as solar cells, thermoelectric devices and mechanical generators—have specific environmental requirements that restrict where they can be deployed and limit their potential for continuous energy production^{3–5}. The ubiquity of atmospheric moisture offers an alternative. However, existing moisture-based energy-harvesting technologies can produce only intermittent, brief (shorter than 50 seconds) bursts of power in the ambient environment, owing to the lack of a sustained conversion mechanism^{6–12}. Here we show that thin-film devices made from nanometre-scale protein wires harvested from the microbe *Geobacter sulfurreducens* can generate continuous electric power in the ambient environment. The devices produce a sustained voltage of around 0.5 volts across a 7-micrometre-thick film, with a current density of around 17 microamperes per square centimetre. We find the driving force behind this energy generation to be a self-maintained moisture gradient that forms within the film when the film is exposed to the humidity that is naturally present in air. Connecting several devices linearly scales up the voltage and current to power electronics. Our results demonstrate the feasibility of a continuous energy-harvesting strategy that is less restricted by location or environmental conditions than other sustainable approaches.

The ubiquity of atmospheric moisture has generated interest in developing moisture-based energy-harvesting technologies^{6–14}. In one strategy, the moisture gradients near sources of liquid water drive microfluidic or nanofluidic water transport in thin films in order to induce charge transport for electric output^{6–10,13}. However, this approach is limited to environments in which there is a liquid water source, and may be difficult to scale up. Alternatively, ambient humidity can generate a vertical gradient of ionized mobile charge (for example, of H⁺ ions) in carbon materials engineered with a heterogeneous vertical distribution of hydroxyl groups^{11,12}. But the power output of ambient-humidity-driven devices has so far produced only brief (shorter than 50-s) bursts of current (of around 0.9 $\mu\text{A cm}^{-2}$, or a power density of about 30 $\mu\text{W cm}^{-3}$) before the device voltage collapses¹². Re-establishing the voltage (to around 0.2 V, or about 20 V cm^{-1}) through self-recharging takes more than 100 s. Thus, the charging time greatly exceeds the duration of power output.

Here, we fabricated an electric generator from a thin film of protein nanowires that produces continuous current for at least 20 h before self-recharging, with a more than two orders of magnitude improvement in power density (to roughly 4 mW cm^{-3}) compared with previous energy-harvesting technologies that rely on ambient, atmospheric moisture. The device consists of a thin (roughly 7- μm) film of protein nanowires deposited on a gold electrode (with an area of around 25 mm^2) patterned on glass (Fig. 1a). The protein nanowires are electrically conductive, and

are sheared from the microorganism *G. sulfurreducens*^{15–17}. A smaller gold electrode (of around 1 mm^2) is placed on top of the nanowire film (Fig. 1a and Supplementary Fig. 1).

Transmission electron microscopy (TEM) images of dried nanowire preparations suggest that the wires (of size 3 $\text{nm} \times 1\text{--}3 \mu\text{m}$) form a mesh network in the film (Fig. 1a and Supplementary Fig. 1). The current–voltage (I – V) curve between the two electrodes shows approximately linear behaviour (Fig. 1b), which is consistent with the ohmic behaviour observed previously in protein-nanowire networks and individual nanowires^{18,19}. However, the I – V curve did not pass through the origin. The open-circuit voltage (V_o) was around 0.5 V and the short-circuit current (I_{sc}) was roughly -250 nA . The effect was robust and highly reproducible, with a uniform V_o ($0.53 \pm 0.03 \text{ V}$, $N = 16$) from different devices of the same film thickness. Outputs were similar in the dark, indicating the lack of a photovoltaic effect (Fig. 1b). Instead, a reduction in relative humidity reduced V_o and I_{sc} (Supplementary Fig. 2). Both V_o and I_{sc} lasted for more than 12 h (Supplementary Fig. 3), indicating that the power output was not a transient phenomenon caused by a charging effect during the measurement. Moreover, the gold electrodes would not be expected to generate current through electrochemical reactions. Similar voltages were generated with inert carbon electrodes (Supplementary Fig. 4), providing additional evidence that the electrode material was not contributing to the observed voltage. Further quantifications and analyses ruled out the possibility that chemical

¹Department of Electrical and Computer Engineering, University of Massachusetts, Amherst, MA, USA. ²Department of Microbiology, University of Massachusetts, Amherst, MA, USA.

³Department of Chemistry, University of Massachusetts, Amherst, MA, USA. ⁴Institute for Applied Life Sciences (IALS), University of Massachusetts, Amherst, MA, USA. ⁵Department of Biochemistry and Molecular Biology, University of Massachusetts, Amherst, MA, USA. ✉e-mail: juny@umass.edu

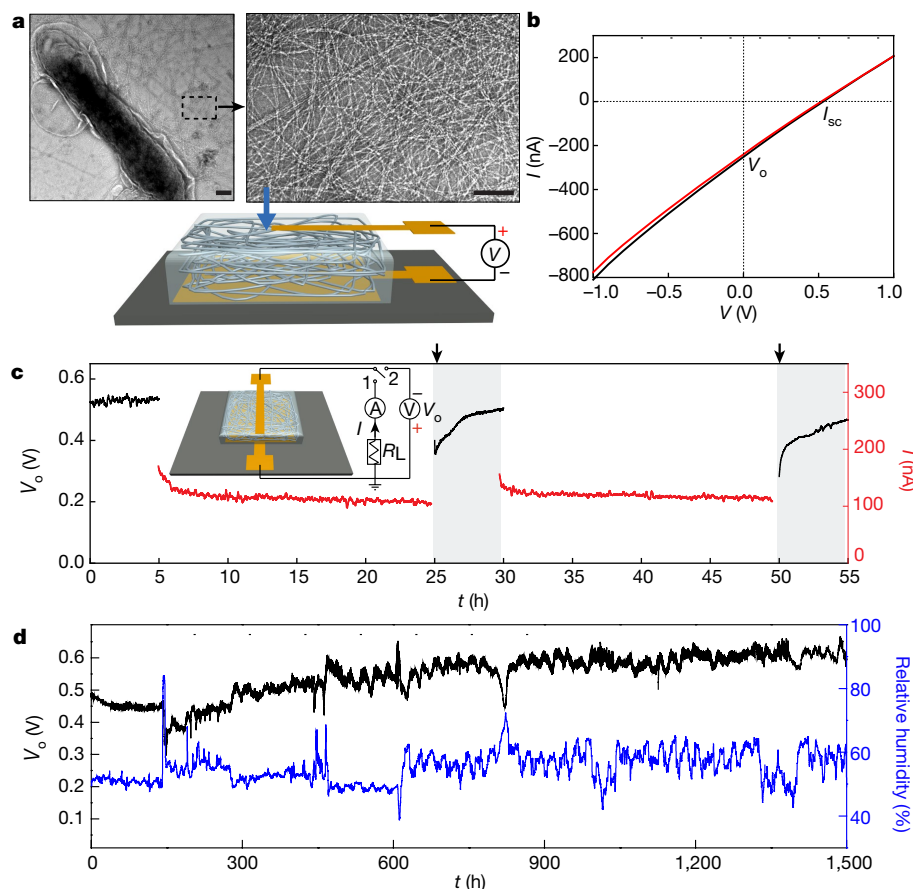


Fig. 1 | Nanowire devices and electric output. **a**, Top, TEM images of the purified nanowire network (right panel) produced by the microorganism *Geobacter sulfurreducens* (dark shape in the left panel). Scale bars, 100 nm. Bottom, diagram of the device structure. **b**, Typical I - V curves from the device with ambient lighting (red) and in the dark (black) at an ambient relative humidity of about 50%. **c**, Evolution of I (red) and V_o (black) from a nanowire device in the ambient environment (at a relative humidity of about 50%). The device initially had a V_o of approximately 0.52 V (at times from 0 to 5 h). Connecting to a load resistor ($R_L = 2$ M Ω) yielded a continuous and gradually stabilized I of about 110 nA for 20 h (red curve; 5 h to 25 h). Then R_L was

disconnected and V_o was recorded (indicated by the arrow at $t = 25$ h). V_o gradually increased to the initial value of 0.5 V (from 25 h to 30 h), showing a self-recharging process. Reconnecting to R_L yielded a repeated continuous powering to the R_L (I is approximately 115 nA) (red curve; 30–50 h). Disconnecting the R_L yielded a second self-recharging process (50–55 h), which brought V_o back to 0.5 V again. The inset shows the circuit diagram, in which connections to terminals 1 and 2 correspond to I and V_o measurements, respectively. **d**, A continuous recording of V_o from a device for more than two months. The ambient relative humidity (blue curve) was also recorded.

decomposition in the protein nanowires was the source of energy of the observed electrical outputs (Supplementary Figs. 5, 6). Removal of oxygen or nitrogen from the gas phase had no impact on voltage generation (Supplementary Fig. 7).

Analysis of current through a load resistor further demonstrated continuous current production for more than 20 h (Fig. 1c). After 20 h of current production the voltage had declined from around 0.5 V to 0.35 V, but was restored to 0.5 V within 5 h (Fig. 1c). Harvesting electric energy through the resistor for an additional 20 h again slightly reduced the voltage, which could be repeatedly self-recharged (Fig. 1c). These results are a substantial improvement over the transient current (of shorter than 50 s) in previous ambient environment generators¹², with a more than hundredfold greater power output. The currents varied with different load resistances, consistent with typical output from an electric power source (Supplementary Fig. 8).

In longer-term monitoring, the device maintained a stable direct-current voltage of some 0.4–0.6 V for more than 2 months (1,500 h; Fig. 1d). Fluctuations in voltage were associated with changes in the ambient relative humidity in the laboratory environment (Fig. 1d). Both the field amplitude (of about 700 V cm⁻¹) and the sustainability of the voltage represented a more than tenfold improvement over the best results from previous ambient generators (for example, roughly 40 V cm⁻¹ for

120 h)^{11,12}. In a controlled humidity environment, a relative humidity of some 40–50% yielded the highest voltage, but substantial voltages were still generated at a relative humidity as low as 20% (comparable to a desert environment) as well as at 100% humidity (Supplementary Fig. 9). This output trend contrasts with that of carbon-based ambient electric generators, which showed a unidirectional increase in output voltage with increasing relative humidity^{11,12}.

The moisture adsorption ratio, W_{H_2O} (the weight of adsorbed moisture divided by the total film weight), measured with a quartz crystal microbalance (Supplementary Fig. 10), was inversely proportional to the film thickness (d), reaching approximately 27% for thin films (of less than 1 μ m) and approximately 15% for thick ones (of more than 8 μ m) (Fig. 2a). This result is consistent with our analysis of a vertical moisture gradient in the film (Fig. 2b), with a W_{H_2O} of around 27% at the surface (at a depth of less than 1 μ m) and of approximately 3% at the bottom (at a depth of more than 8 μ m), yielding the observed overall W_{H_2O} of roughly 15% in thick films. The moisture gradient, or rather a depth-dependent local adsorption, in the film was confirmed by our observation and analysis of increased adsorption in films with both interfaces exposed (Supplementary Fig. 11). Modelling this apparent difference in moisture adsorption (ΔW_{H_2O}) between the top (exposed) and bottom (sealed) interfaces demonstrated a clear correspondence between

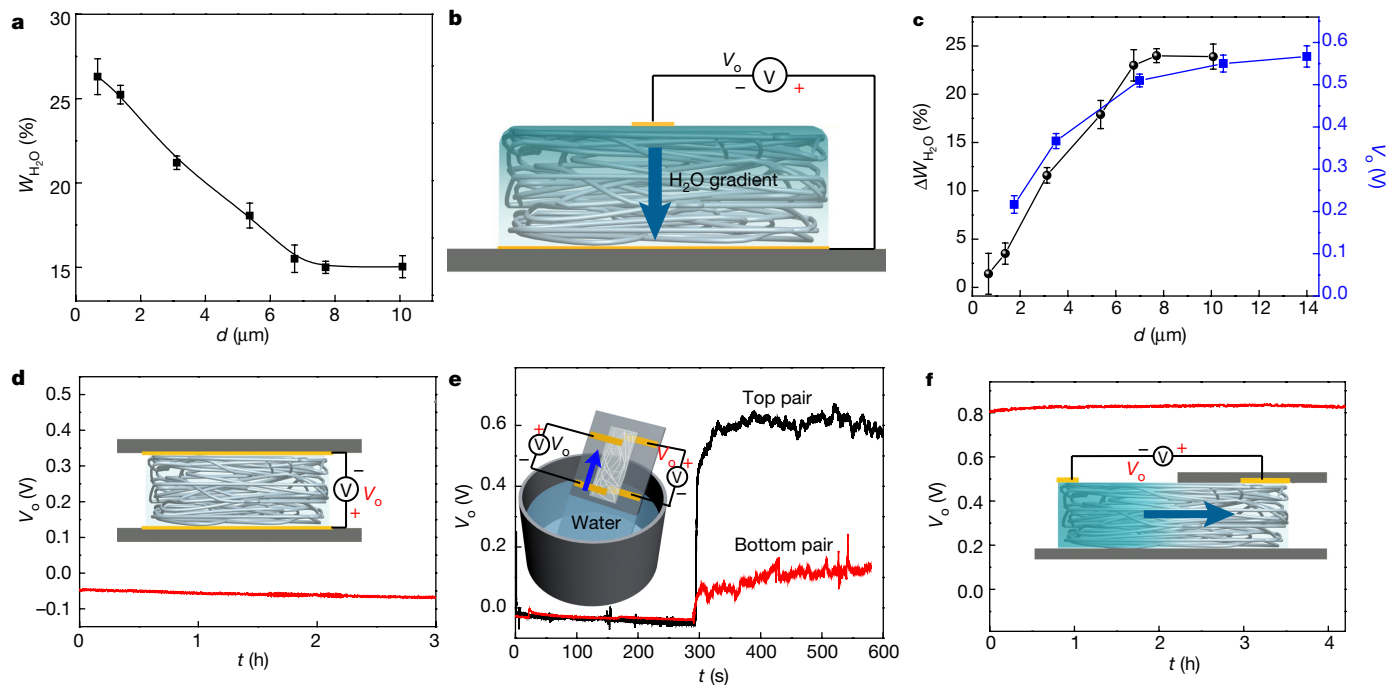


Fig. 2 | Moisture gradient in nanowire film and electric output. **a**, $W_{\text{H}_2\text{O}}$ in nanowire films is plotted against film thickness (d) at an ambient relative humidity of roughly 50%. **b**, Diagram showing a vertical moisture gradient in the nanowire film. **c**, $\Delta W_{\text{H}_2\text{O}}$ and output voltage (V_o) plotted against d . $\Delta W_{\text{H}_2\text{O}} = 2 \times (27\% - W_{\text{H}_2\text{O}})$ is the estimated difference in moisture-adsorption ratios between the top and bottom interfaces. **d**, A residual V_o of roughly -0.05 V is produced by a symmetric nanowire device with both top and bottom surfaces sealed. **e**, Inset, diagram of a nanowire device (area 1×2 cm², thickness

roughly 7 μm) aligned vertically with the moisture gradient (blue arrow) above the water surface, with a pair of electrodes placed at either the top or the bottom interface. The V_o from the top (black) and bottom (red) pairs of electrodes changed (at times longer than 300 s) after the devices were placed close to the water surface. **e**, A residual V_o of about 0.8 V is measured from a pair of top electrodes in a nanowire device with half of the top surface covered by a glass slide. The error bars in **a**, **c** represent the standard deviation of the statistical means from multiple measurements (n is 3 or more).

increasing $\Delta W_{\text{H}_2\text{O}}$ and increasing V_o , up to a plateau of roughly 0.55 V for thick films with d values of approximately 10 μm (Fig. 2c). Moisture contents, and thus presumably the proposed moisture gradients, remained stable over time (Supplementary Fig. 12), consistent with the long-term stability of V_o (Fig. 1d). The moisture gradient built up from a non-gradient ambient environment renders our films fundamentally different to all previous moisture-based technologies that lack this capability^{6–14}. This indicates an intrinsically different mechanism for sustained power generation.

Further evidence for the importance of the adsorption-difference-induced moisture gradient in generating voltage was the observation that a voltage was not generated when the top film was completely covered with a gold electrode (Fig. 2d). Near-zero voltages were obtained when two electrodes were placed on top of the film. However, if the film was positioned vertically over water to produce a moisture gradient between the two top electrodes, then a voltage was produced (Fig. 2e). A pair of electrodes placed underneath the film produced a considerably smaller voltage, consistent with the expected lower moisture adsorption at depth (Fig. 2e). Alternatively, creating an adsorption difference and hence a moisture gradient between two top electrodes by covering a portion of the film with a glass slide also generated a stable voltage (Fig. 2f). Reducing the moisture gradient by driving water out of the film with heat reduced the voltage across the film; as the film rehydrated, the voltage was restored (Supplementary Fig. 13).

The protein nanowires, which may have several compositions^{17,20,21}, have non-uniform diameters with periodic surface structures along the axis^{20–23}. As a result, we expect nanometre-scale pores or nanopores to form at nanowire–nanowire interfaces in a nanowire film. Molecular-dynamics simulations support the assumption that, even in the most compact stacking configurations of different wires, there are still nanopores that allow for the passage of water molecules

(Supplementary Fig. 14). In a real film, the nanowires are randomly distributed (Supplementary Fig. 1c, e), indicating a wide distribution of nanopores. The presence of a high density of these nanopores in the film helps to account for the existence of a moisture gradient. Specifically, a lowering of vapour pressure is generally observed in a porous medium owing to the contribution of a capillary pressure, and the effect is stronger for smaller pore sizes²⁴. In fact, for water vapour, a substantial effect can be observed only with a nanometre-scale pore size²⁴. At steady state, it is expected that a vapour-pressure gradient must exist at the air–material interface (Fig. 3a). For a thin nanowire film (of less than 7 μm , for instance), the entire thickness is expected to be within this interfacial vapour-pressure gradient, whereas a thicker film extends outside of the finite gradient region. Water adsorption at a solid surface is a dynamic equilibrium involving constant adsorption–desorption exchange at the interface^{25–27}. In general recombination dynamics²⁸, the adsorption is expected to be proportional to molecular concentration of water molecules in air or the vapour pressure. As a result, the induced vapour-pressure gradient in the nanowire film will lead to a moisture gradient, as we observe (Fig. 2a). Saturation in the vapour-pressure difference for a thicker film leads to a saturation in moisture-adsorption difference ($\Delta W_{\text{H}_2\text{O}}$) that is also consistent with our experimental observations (Fig. 2c).

This moisture gradient can account for the voltage generation in our nanowire films. The surface functional groups (for example, carboxylic groups) innate to the nanowires are a source of exchangeable protons^{20–23}. The moisture gradient is expected to create an ionization gradient in the carboxylic groups or a concentration gradient in mobile protons (against an immobile COO^- anionic background). The proton gradient leads to the diffusion of protons, possibly facilitated by a hole-like conduction in the nanowire¹⁸. This charge diffusion is expected to induce a counterbalancing electrical field or potential analogous to

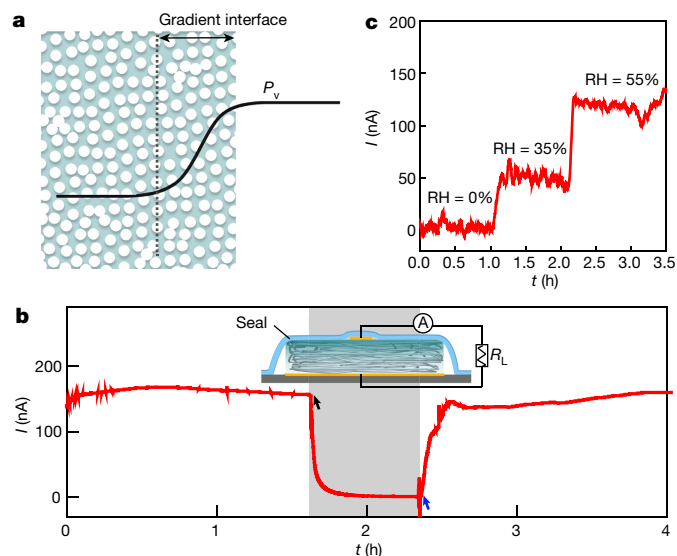


Fig. 3 | Mechanisms for electric output. **a**, Diagram showing a lowering of vapour pressure (P_v) in a porous material and the existence of a vapour-pressure gradient close to the air interface. **b**, Continuous current output from a nanowire device in the ambient environment (relative humidity roughly 45%) is disrupted (black arrow) when the top interface is covered with a parafilm (inset). The current disruption persists (grey region) until the seal is removed, when the current begins to return to its original value (blue arrow). $R_L = 2 \text{ M}\Omega$. **c**, Current output from a nanowire device at different relative humidities (RH).

the resting membrane potential in biological systems²⁹. Our experimental observations show that the lower-moisture side always had a higher (positive) potential (Figs. 1, 2), consistent with the predictions of this diffusion model (Supplementary Figs 15, 16). In particular, the

diffusion dynamics implies that the built-up voltage is proportional to the difference in proton concentration¹², which is considered to be closely related to $\Delta W_{\text{H}_2\text{O}}$ (Supplementary Fig. 13). This is again consistent with our experimental observation that $\Delta W_{\text{H}_2\text{O}}$ correlates closely with output voltage (Fig. 2c). A maintained moisture gradient, which is fundamentally different to anything seen in previous systems^{6–14}, explains the continuous voltage output from our nanowire device (Fig. 1d).

The analyses above indicate that a high density of nanopores is key to forming the moisture gradient, and that a high density of surface functional groups subsequently leads to a potential gradient by charge diffusion in the film. Control devices made from other porous thin films, which feature either larger pore sizes³⁰ or nanoscale pores without functional groups, did not yield electric output (Supplementary Fig. 17). Thin films made from a nanowire derivative, Aro-5—in which the amino acid alanine is substituted for aromatic amino-acid groups, but which still maintains a similar wire structure and a high density of carboxyl groups³¹—yielded similar electric output (Supplementary Fig. 18). This positive control indicates that a wide range of synthetic protein nanowires^{19–21} is likely to satisfy both the chemical and the structural requirements for electric output. We further substantiated the device performance intrinsic to the material properties by excluding side effects (for example, an effect of pH) from the preparation solution. Nanowire films prepared from close-to-neutral solution yielded similar electric output (Supplementary Fig. 19), whereas films made of other materials prepared in low-pH solutions did not yield an electric output (Supplementary Fig. 20).

We experimentally determined that the ambient humidity was the source of energy input to the nanowire device. First, we found that blocking water-molecule exchange at the nanowire–air interface by sealing the top interface of the nanowire film drained the electric output, whereas removing this seal restored continuous output (Fig. 3b). Second, increasing the water-molecule exchange rate by increasing

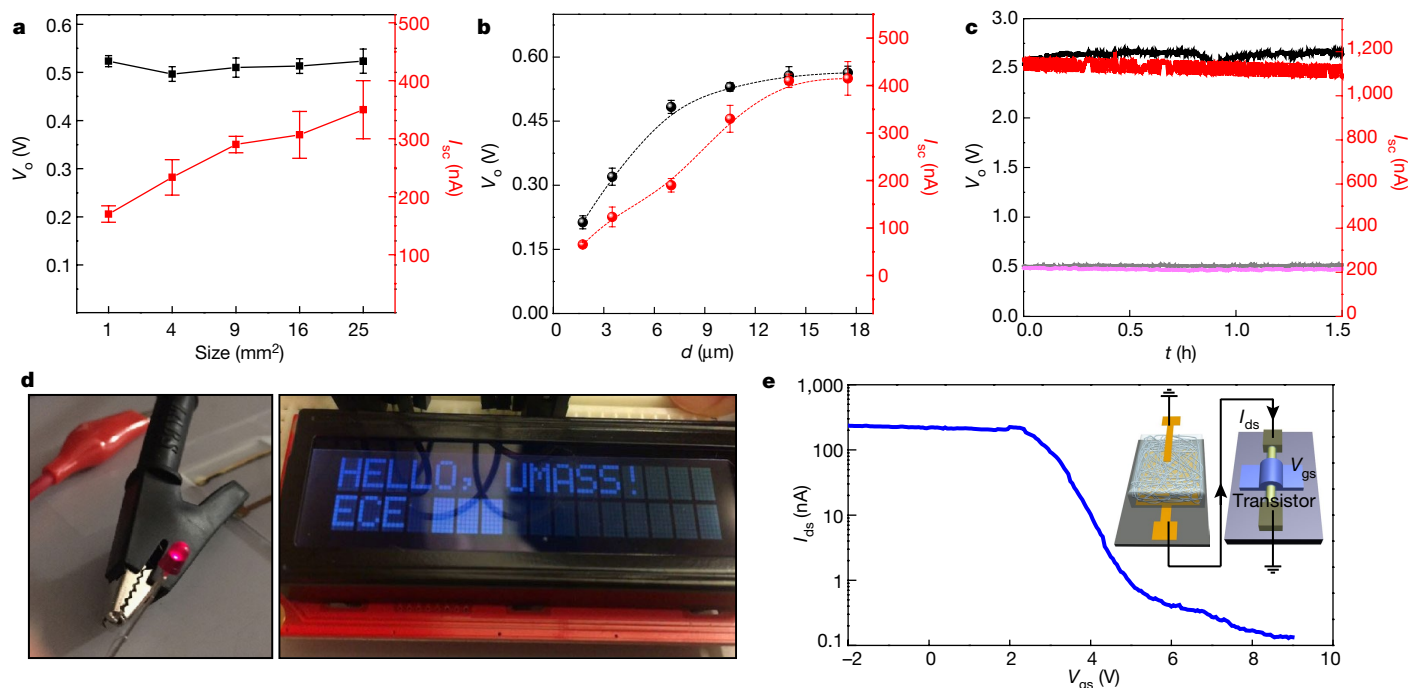


Fig. 4 | Powering from nanowire devices. **a**, V_o (black) and I_{sc} (red) plotted against device size at an ambient relative humidity of about 50%, for a film thickness of roughly $7 \mu\text{m}$. **b**, V_o (black) and I_{sc} (red) plotted against film thickness (d) at an ambient relative humidity of about 50%, for a film size of roughly 1 mm^2 . **c**, V_o (black) and I_{sc} (red) obtained by connecting five nanowire devices in series and in parallel, respectively, compared with V_o (grey) and I_{sc} (purple) from an individual nanowire device. **d**, The nanowire devices were used to charge up capacitors to power a LED (left) or an LCD panel (right). **e**, Source–drain current (I_{ds}) with respect to gate voltage (V_{gs}) from a Ge/Si nanowire transistor powered by a nanowire device. The inset shows the circuit diagram. The error bars in **a**, **b** represent the standard deviation of the statistical means from multiple measurements (n is 3 or more).

the relative humidity correspondingly increased the electric output (Fig. 3c), which was also reversible (Supplementary Fig. 21).

We therefore propose the following qualitative mechanism for energy harvesting in the nanowire film. Water molecules in air naturally comprise ionized species^{25–27}, or are ionized when adsorbed on the nanowire surface. The ionized clusters (for example, $\text{H}(\text{H}_2\text{O})_n^+/\text{HO}(\text{H}_2\text{O})_n^-$) donate charge (for example, H^+/e^-) to the nanowire, supplying the closed-loop current flow driven by the voltage resulting from the moisture gradient. A dynamic adsorption–desorption exchange of water molecules at the interface provides a continuous input. The ambient environment provides a large reservoir for this continuous exchange of water molecules to generate a sustained electric output (Fig. 1c). This mechanistic picture is consistent with previous findings of spontaneous surface charging on solid interfaces by atmospheric moisture^{25–27}. Our nanowires seem to yield a particularly efficient charge transfer for continuous electric output, probably because of collective effects from surface groups with high affinity for water molecules and a self-maintained electric field that facilitates ionization and charge transfer. Future studies are required to determine the specific charge species and associated transfer processes.

Our device can be reduced in size, and several devices can be connected in series or in parallel to linearly increase the output voltage or current. A V_0 of around 0.5 V is maintained even with a device size as small as 1 mm² or so (Fig. 4a), whereas I_{sc} gradually decreases to some 170 nA. The reduction in I_{sc} is a direct result of the nonlinear increase in the film resistance between a pair of asymmetric electrodes (Supplementary Fig. 22). The areal power density (estimated by $(V_0 I_{sc})/4$) increases with the increase in film thickness and saturates at roughly 5 $\mu\text{W cm}^{-2}$ at a film thickness of about 14 μm (Fig. 4b), consistent with the trend in voltage output (Fig. 2c). This power output is estimated to be around 4% of the theoretical upper limit (Supplementary Fig. 23). The converted volumetric power density of about 4 mW cm⁻³ is more than two orders of magnitude larger than the power density obtained in previous carbon-based systems^{11,12}. As ambient humidity diffuses over three dimensions, stacking thin-film devices in the vertical direction with a 1/1 film/airgap ratio can lead to a practical volumetric power density of more than 1 kW m⁻³ (Supplementary Fig. 24), potentially outperforming solar cells, which are intrinsically surface confined². The devices could be connected in series or in parallel to linearly increase the output voltage or current (Fig. 4c); we found that a voltage of 10 V was achieved by connecting 17 devices in series (Supplementary Fig. 25). Connected devices charged a capacitor to power a LED (Fig. 4d, left) or a LCD (Fig. 4d, right, and Supplementary Fig. 26). A single device could power a semiconductor nanowire transistor^{32,33} for logic operation (Fig. 4e, Supplementary Fig. 27), demonstrating typical *p*-type transport behaviours. Logic control and signal amplification without an external power supply could lead to low-cost, self-sustained and environment-driven sensing and computing systems.

Online content

Any methods, additional references, Nature Research reporting summaries, source data, extended data, supplementary information, acknowledgements, peer review information; details of author contributions and competing interests; and statements of data and code availability are available at <https://doi.org/10.1038/s41586-020-2010-9>.

1. Tentzeris, M. M., Georgiadis, A. & Roselli, L. Energy harvesting and scavenging. *Proc. IEEE* **102**, 1644–1648 (2014).
2. Abowd, G. D. & Mynatt, E. D. Charting past, present, and future research in ubiquitous computing. *ACM Trans. Comput. Hum. Interact.* **7**, 29–58 (2000).
3. Parida, B., Iniyar, S. & Goic, R. A review of solar photovoltaic technologies. *Renew. Sustain. Energy Rev.* **15**, 1625–1636 (2011).
4. Wang, Z. L. Triboelectric nanogenerators as new energy technology for self-powered systems and active mechanical and chemical sensors. *ACS Nano* **7**, 9533–9557 (2013).
5. Champier, D. Thermoelectric generators: a review of applications. *Energy Convers. Manage.* **140**, 167–181 (2017).
6. Zhao, F., Cheng, H., Zhang, Z., Jiang, L. & Qu, L. Direct power generation from a graphene oxide film under moisture. *Adv. Mater.* **27**, 4351–4357 (2015).
7. Xue, J. et al. Vapor-activated power generation on conductive polymer. *Adv. Funct. Mater.* **26**, 8784–8792 (2016).
8. Zhao, F., Liang, Y., Cheng, H., Jiang, L. & Qu, L. Highly efficient moisture-enabled electricity generation from graphene oxide frameworks. *Energy Environ. Sci.* **9**, 912–916 (2016).
9. Ding, T. et al. All-printed porous carbon film for electricity generation from evaporation-driven water flow. *Adv. Funct. Mater.* **27**, 1700551 (2017).
10. Shen, D. et al. Self-powered wearable electronics based on moisture enabled electricity generation. *Adv. Mater.* **30**, 1705925 (2018).
11. Liu, K. et al. Induced potential in porous carbon films through water vapor adsorption. *Angew. Chem. Int. Edn* **55**, 8003–8007 (2016).
12. Cheng, H. et al. Spontaneous power source in ambient air of a well-directionally reduced graphene oxide bulk. *Energy Environ. Sci.* **11**, 2839–2845 (2018).
13. Xue, G. et al. Water-evaporation-induced electricity with nanostructured carbon materials. *Nat. Nanotechnol.* **12**, 317–321 (2017).
14. Zhang, Z. et al. Emerging hydrovoltaic technology. *Nat. Nanotechnol.* **13**, 1109–1119 (2018).
15. Lovley, D. R. Electrically conductive pili: biological function and potential applications in electronics. *Curr. Opin. Electrochem.* **4**, 190–198 (2017).
16. Lovley, D. R. e-Biologics: fabrication of sustainable electronics with “green” biological materials. *MBio* **8**, e00695 (2017).
17. Lovley, D. R. & Walker, D. J. F. Geobacter protein nanowires. *Front. Microbiol.* **10**, 2078 (2019).
18. Malvankar, N. S. et al. Tunable metallic-like conductivity in microbial nanowire networks. *Nat. Nanotechnol.* **6**, 573–579 (2011).
19. Adhikari, R. Y., Malvankar, N. S., Tuominen, M. T. & Lovley, D. R. Conductivity of individual Geobacter pili. *RSC Adv.* **6**, 8354–8357 (2016).
20. Filman, D. J. et al. Cryo-EM reveals the structural basis of long-range electron transport in a cytochrome-based bacterial nanowire. *Commun. Biol.* **2**, 219 (2019).
21. Wang, F. et al. Structure of microbial nanowires reveals stacked hemes that transport electrons over micrometers. *Cell* **177**, 361–369 (2019).
22. Feliciano, G. T., Steidl, R. J. & Reguera, G. Structural and functional insights into the conductive pili of *Geobacter sulfurreducens* revealed in molecular dynamics simulations. *Phys. Chem. Chem. Phys.* **17**, 22217 (2015).
23. Xiao, K. et al. Low energy atomic models suggesting a pilus structure that could account for electrical conductivity of *Geobacter sulfurreducens* pili. *Sci. Rep.* **6**, 23385 (2016).
24. Ho, C. K. & Webb, S. W. *Gas Transport in Porous Media* (Springer, 2006).
25. Soares, L. C., Bertazzo, S., Burgo, T. A. L., Baldim, V. & Galembek, F. A new mechanism for the electrostatic charge build-up and dissipation in dielectrics. *J. Braz. Chem. Soc.* **19**, 277–286 (2008).
26. Gouveia, R. F. & Galembek, F. Electrostatic charging of hydrophilic particles due to water adsorption. *J. Am. Chem. Soc.* **131**, 11381–11386 (2009).
27. Ducati, T. R. D., Simoes, L. H. & Galembek, F. Charge partitioning at gas–solid interfaces: humidity causes electricity buildup on metals. *Langmuir* **26**, 13763–13766 (2010).
28. Perkins, R. S. Rate laws for elementary chemical reactions. *J. Chem. Educ.* **51**, 254 (1974).
29. Wright, S. H. Generation of resting membrane potential. *Adv. Physiol. Educ.* **28**, 139–142 (2004).
30. Yin, B., Liu, X., Gao, H., Fu, T. & Yao, J. Bioinspired and bristled microparticles for ultrasensitive pressure and strain sensors. *Nat. Commun.* **9**, 5161 (2018).
31. Vargas, M. et al. Aromatic amino acids required for pili conductivity and long-range extracellular electron transport in *Geobacter sulfurreducens*. *MBio* **4**, e00105-13 (2013); erratum **4**, e00210-13 (2013).
32. Xiang, J. et al. Ge/Si nanowire heterostructures as high-performance field-effect transistors. *Nature* **441**, 489–493 (2006).
33. Yao, J. et al. Nanowire nanocomputer as a finite-state machine. *Proc. Natl Acad. Sci. USA* **111**, 2431–2435 (2014).

Publisher's note Springer Nature remains neutral with regard to jurisdictional claims in published maps and institutional affiliations.

© The Author(s), under exclusive licence to Springer Nature Limited 2020

Methods

Synthesis and purification of protein nanowires

Geobacter sulfurreducens was routinely cultured at 25 °C under strict anaerobic conditions (80/20 N₂/CO₂) in chemostats³⁴ in a previously described³⁵ mineral-based medium containing acetate (15 mM) as the electron donor and fumarate (40 mM) as the electron acceptor. Cells were collected with centrifugation and resuspended in 150 mM ethanolamine buffer (pH 10.5). The nanowires were harvested and purified as described³⁶. Briefly, protein nanowires were sheared from the cells in a blender. Cells were removed by centrifugation. The nanowires in the supernatant were precipitated with ammonium sulfate followed by centrifugation. The precipitate was resuspended in ethanolamine buffer and additional debris was removed by centrifugation. Nanowires were collected with a second 10% ammonium sulfate precipitation and subsequent centrifugation at 13,000g. The nanowires were resuspended in ethanolamine buffer. This nanowire preparation was dialysed against deionized water to remove the buffer and stored at 4 °C.

Fabrication of protein-nanowire devices

The bottom electrode (Cr/Au, 10/100 nm) was first defined on a glass slide (25 × 75 mm²; Fisher Scientific) by standard metal electron-beam evaporation using a shadow mask. A polydimethylsiloxane (PDMS, Sylgard 184, 10/1 mix ratio; Dow Corning) film (3–5 mm thick) was cut with an opening (1–25 mm²), which served as the well for holding the nanowire solution and placed on the glass slide with the opening aligned to the defined bottom electrode. The purified nanowire solution was tuned to pH 2.0 with hydrochloric acid (HCl) solution to improve nanowire conductivity³⁷ and drop-casted into the PDMS well. Nanowire film prepared by as-purified, close-to-neutral solution without HCl yielded a similar electric output (Supplementary Fig. 19). The glass slide was then placed on a hot plate (at roughly 80 °C) to facilitate solvent (water) evaporation in order to form the nanowire thin film (Supplementary Fig. 1a). Note that the nanowires have been found to be stable at temperatures higher than 100 °C (ref. 16). The final nanowire-film thickness was controlled by tuning the solution volume over the unit area. Empirically, a 110 μl cm⁻² nanowire solution (150 μg ml⁻¹) yielded an average film thickness of roughly 1 μm. The PDMS mould was removed after nanowire-film assembly. Finally, a confined gold electrode was placed on top of the nanowire film to complete the device structure for electrical measurement. Two forms of top gold electrodes were used (Supplementary Fig. 1g). The first was a braided gold-plated shield (diameter roughly 0.7 mm, model CC-SC-50; LakeShore) and the second was a polyethylene terephthalate (PET) thin-film stripe (roughly 0.5 mm wide) coated with 50-nm gold film. Both top electrodes yielded close electrical outputs. For control protein-nanowire devices using printed carbon electrodes (Supplementary Fig. 4), conductive carbon film was printed using a desktop inkjet printer (DMP-2831, Dimatix; carbon ink JR-700HV, NovaCentrix) on the glass slide and on a paper stripe to form the bottom and top electrodes, respectively.

Germanium–silicon nanowire transistor

We synthesized Ge–Si core-shell nanowires using the gold-nanocluster-catalysed vapour–liquid–solid method described previously^{32,33}. Specifically, a growth substrate (Si substrate with 600-nm thermal SiO₂, Nova Electronics) was first dispersed with gold nanoparticles (10 nm, Ted Pella). Then the growth substrate was placed in a quartz-tube reactor. The Ge core was synthesized at 270 °C and 450 Torr, with 30 standard cubic centimetres per minute (sccm) of germane (GeH₄, 10% in H₂) and 200 sccm H₂ serving as the reactant and carrier gases, respectively. The growth time was about 1 h, yielding Ge nanowires with an average length of around 50 μm and an average diameter of 10 nm. The epitaxial Si shell was grown immediately after the growth of the core at 460 °C and 5 Torr for 2 min, with 5 sccm silane (SiH₄) as the reactant gas. The epitaxial growth yielded an average Si shell thickness

of roughly 2–3 nm, resulting in core–shell nanowires with an overall diameter of roughly 15 nm. Synthesized Ge–Si nanowires were first dispersed in ethanol solution, assisted by a brief ultrasonication. Then the dispersed nanowires were drop-casted onto a Si substrate coated with 600 nm SiO₂ (Nova Electronics). The source and drain contacts of the nanowires were defined by standard electron-beam lithography, followed by the thermal evaporation of metal contacts (Cr/Ni, 1/40 nm) and lift-off process. A tri-layer Al₂O₃/ZrO₂/Al₂O₃ (2/5/5 nm) was deposited by atomic-layer deposition to serve as the top-gate dielectric³³. The top-gate contact was defined by standard electron-beam lithography, thermal evaporation of metals (Cr/Au, 4/65 nm), and a lift-off process.

Electrical measurements

Electrical measurements were performed in an ambient environment, unless otherwise specified. The output voltage (V_o) in the nanowire devices was first buffered by a unit-gain amplifier (LM741; Texas Instruments) and the short-circuit current (I_{sc}) was amplified with a preamplifier (DL-1211; DL Instruments). Both signals were then recorded at an acquisition rate of 10–100 Hz using a 16-channel A/D converter (Digidata 1440A; Molecular Devices) interfaced with a computer running recording software. We used a unit-gain amplifier (LM741; Texas Instruments) for voltage-signal buffering because the nanowire devices have an internal resistance in the range of MΩ (Fig. 1b), which is comparable to the input resistance of the A/D converter (roughly 1 MΩ), so a direct connection would induce measurement error. The relative humidity in the ambient environment was recorded by using a humidity datalogger (R6030; Reed Instruments). The I – V sweep in the nanowire devices was performed using a source meter (Keithley 2401; Tektronix) interfaced with computerized recording software. The transfer characteristics in the Ge–Si nanowire transistors were measured using a semiconductor characterization system (Keithley 4200-SCS; Tektronix). Individual capacitors (CAPXON Electrolytic Capacitors; 1,000 μF, 16 V) were charged by nanowire devices with an average voltage output of approximately 0.55 V. The LCD (ADM1602K-NSW-FBS/3.3 V; Sparkfun Electronics) was lit by ten capacitors in series and the LED (630-HLMP-K150; Mouser Electronics) was lit by four capacitors in series.

Humidity control

For some specific device characterizations, we varied the relative humidity through two approaches. First, carrier gases (for example, N₂, O₂, air) bubbling through a water-containing conical flask were led into a gas-purge desiccator cabinet (H42053-0002; Bel-Art), and the flow rate was adjusted to control the relative humidity in the desiccator cabinet. The relative humidity was monitored in real time using a hygrometer (model 8706; Reed Instruments). We used the bubbler method to control the relative humidity in different gas environments (Supplementary Fig. 7) and for moisture adsorption measurements (Supplementary Fig. 10). Alternatively, we controlled the relative humidity by tuning the equilibrium vapour pressure of sulfuric acid solutions, that is, the concentration of sulfuric acid³⁸. We used the equilibrium-vapour method to stabilize the relative humidity over the long term (Fig. 1c), to change the relative humidity instantly (Fig. 3b, c and Supplementary Fig. 21), and to produce wide-range relative humidities (Supplementary Fig. 9).

Imaging

We measured the thickness of protein-nanowire films using a desktop scanning electron microscope (SEM, EM-30 Plus; Element Pi). We took optical images of the Ge–Si nanowire device using an upright microscope (Olympus BH2-UMA). We imaged the nanowire networks using a transmission electron microscope (JEM-2200FS, JEOL). The bonding spectra in protein nanowires were characterized by Fourier-transform infrared spectroscopy (FTIR; Perkin Elmer) with a universal attenuated-total-reflection (ATR) sampling accessory.

Molecular-dynamics simulation

Atomistic molecular-dynamics simulations of the protein nanowires were performed using the CHARMM program³⁹ with the latest CHARMM 36m force field⁴⁰. The initial structure was obtained from previous modelling work²³. We included 12 monomers, which is sufficient to provide an intact filament environment for the flexible carboxy-terminal tails of the first six monomers (Supplementary Fig. 14). Simulations were performed in the vacuum phase, which mimics the fully dehydrated state of the film, to examine the nanoscale water-permeable pores that may be formed in a nanowire network (Supplementary Fig. 14). Consistent with the vacuum condition, all glutamate, aspartate, lysine and arginine amino acids were simulated in their neutral states. Inspired by the TEM images, we focused primarily on parallel configurations in which the filaments would achieve the tightest packing.

We carried out 588 simulations, in which the relative positions of the two filaments were shifted along two directions—parallel or perpendicular to the filament axis—and one of the filaments was rotated along the filament axis (Supplementary Fig. 14a). One filament was defined as the reference filament, and the other was mobile. We set up 21 windows along the direction of the filament axis, with the relative shift of two filaments ranging from -4 nm to 4 nm with a spacing of 0.4 nm. At each shift along the filament axis, four windows were used along the direction perpendicular to the filament axis, with the relative distance between two filaments varying between 3.3 nm and 4.2 nm with an interval of 0.3 nm. Seven windows were used for the rotation of one filament, with rotation angles between 0 and 60° with an interval of 10° . At each window, molecular-dynamics simulations were performed to equilibrate interfilament interfacial packing. During molecular-dynamics equilibration, all C α atoms of the helical core segment (residues 4–50) were fixed, in order to maintain the integrity of both filaments and to minimize modelling error due to undesired structural changes. Each system was first energy minimized for 2,000 steps, and then slowly heated from 100 K to 300 K in 5,000 steps. Production simulations were performed under 300 K for 3 ns. During analysis, the first half of each trajectory was discarded as the equilibration process, and the averaged potential energy was computed for each window. This allowed us to identify the interfilament distance and filament rotation with the minimal averaged potential energy for each shift distance along the filament axis. The maximum enclosed pore was then analysed using the HOLE program⁴¹ for the most stable configuration identified at each shift along the filament axis.

We also used similar approaches to examine the formation of water-permeable pores in OmcS–OmcS filaments and OmcS–*pili* filaments. In both cases, one OmcS filament was defined as the reference filament, and the other was mobile (Supplementary Fig. 14b, c). We set up 21 windows along the direction of the filament axis, with the relative shift of two filaments ranging from -10 nm to 0 nm with a spacing of 0.5 nm. Given that the OmcS filament showed a sinusoidal shape with a period of around 20 nm (refs. ^{20,21}), we expect that the pore radii as a function

of their relative shift in this direction will be symmetric with respect to a relative shift of 0 nm. At each shift along the filament axis, we used six windows along the direction perpendicular to the filament axis, with the relative distance between two filaments varying between 4.2 nm and 5.7 nm with an interval of 0.3 nm in this direction. In the system of OmcS–OmcS filaments, we used nine windows for the rotation of one filament, with rotation angles between 0 and 80° with an interval of 10° . In the system of OmcS–*pili* filaments, we used seven rotational windows with rotation angles ranging from 0 to 60° with a spacing of 10° .

Data availability

The data that support the findings of this study are available within the paper and Supplementary Information. Additional supporting data generated during the present study are available from the corresponding author upon reasonable request.

- Esteve-Núñez, A., Rothermich, M. M., Sharma, M. & Lovley, D. R. Growth of *Geobacter sulfurreducens* under nutrient-limiting conditions in continuous culture. *Environ. Microbiol.* **7**, 641–648 (2005).
- Coppi, M. V., Leang, C., Sandler, S. J. & Lovley, D. R. Development of a genetic system for *Geobacter sulfurreducens*. *Appl. Environ. Microbiol.* **67**, 3180–3187 (2001).
- Tan, Y. et al. Expressing the *Geobacter metallireducens* PIIA in *Geobacter sulfurreducens* yields pili with exceptional conductivity. *MBio* **8**, e02203-16 (2017).
- Tan, Y. et al. Synthetic biological protein nanowires with high conductivity. *Small* **12**, 4481–4485 (2016).
- Feng, J. et al. Giant moisture responsiveness of VS₂ ultrathin nanosheets for novel touchless positioning interface. *Adv. Mater.* **24**, 1969–1974 (2012).
- Brooks, B. R. et al. CHARMM: the biomolecular simulation program. *J. Comput. Chem.* **30**, 1545–1614 (2009).
- Huang, J. et al. CHARMM36m: an improved force field for folded and intrinsically disordered proteins. *Nat. Methods* **14**, 71–73 (2017).
- Smart, O. S., Neduvetil, J. G., Wang, X., Wallace, B. A. & Sansom, M. S. P. HOLE: a program for the analysis of the pore dimensions of ion channel structural models. *J. Mol. Graph. Model.* **14**, 354–360 (1996).

Acknowledgements J.Y. and D.R.L. acknowledge support from a seed fund through the Office of Technology Commercialization and Ventures at the University of Massachusetts, Amherst. J.C. and Xiaorong L. acknowledge support from the National Institutes of Health (grant GM114300 to J.C.). Part of the device fabrication work was conducted in the Center for Hierarchical Manufacturing (CHM), a National Science Foundation (NSF) Nanoscale Science and Engineering Center (NSEC) located at the University of Massachusetts Amherst.

Author contributions J.Y. and Xiaomeng L. conceived the project and designed experiments. D.R.L. oversaw material design and production. Xiaomeng L. carried out experimental studies. H.G. helped with device fabrication and characterization. J.E.W. performed material synthesis and imaging. Xiaorong L. and J.C. designed the computational study and analysis. Xiaorong L. performed simulations and analysis. B.Y. performed resistance simulations. T.F. helped with electrode fabrication. J.Y. and D.R.L. wrote the paper. All authors discussed the results and implications and commented on the manuscript at all stages.

Competing interests The authors declare no competing interests.

Additional information

Supplementary information is available for this paper at <https://doi.org/10.1038/s41586-020-2010-9>.

Correspondence and requests for materials should be addressed to J.Y.

Peer review information *Nature* thanks Liangti Qu and the other, anonymous, reviewer(s) for their contribution to the peer review of this work.

Reprints and permissions information is available at <http://www.nature.com/reprints>.